BIONSENSORS

Battery-free, wireless sensors for full-body pressure and temperature mapping

Seungyong Han,[1,2]* Jeonghyun Kim,[1,3]* Sang Min Won,[1]* Yinji Ma,[4,5]* Daeshik Kang,[2] Zhaoqian Xie,[4,5] Kyu-Tae Lee,[1] Ha Uk Chung,[6] Anthony Banks,[1] Seunghwan Min,[1] Seung Yun Heo,[6] Charles R. Davies,[7] Jung Woo Lee,[1,8] Chi-Hwan Lee,[9] Bong Hoon Kim,[6] Kan Li,[5] Yadong Zhou,[5,10] Chen Wei,[5] Xue Feng,[4] Yonggang Huang,[5]† John A. Rogers[1,6]†

Thin, soft, skin-like sensors capable of precise, continuous measurements of physiological health have broad potential relevance to clinical health care. Use of sensors distributed over a wide area for full-body, spatiotemporal mapping of physiological processes would be a considerable advance for this field. We introduce materials, device designs, wireless power delivery and communication strategies, and overall system architectures for skin-like, battery-free sensors of temperature and pressure that can be used across the entire body. Combined experimental and theoretical investigations of the sensor operation and the modes for wireless addressing define the key features of these systems. Studies with human subjects in clinical sleep laboratories and in adjustable hospital beds demonstrate functionality of the sensors, with potential implications for monitoring of circadian cycles and mitigating risks for pressure-induced skin ulcers.

INTRODUCTION

Thin, soft, skin-like electronic devices that exploit wireless, near-field communication (NFC) technologies offer simple, battery-free platforms for the continuous monitoring of physiological health (*1*–*6*). Applications range from those in hospital care and clinical medicine to physical rehabilitation, fitness/wellness tracking, awareness and cognitive state assessment, and human-machine interfaces (*7*, *8*). Although use of an individual device on a targeted region of the body enables clinically validated measurement modalities in electrophysiology, temperature, pressure, blood oximetry, and others, using multiple separate devices across different anatomical locations simultaneously could expand the possibilities to enable measurements across the body for tracking of position-dependent body processes, disease states, and/or external stimuli (*8*, *9*).

Mapping the skin temperature and pressure in specific areas of the body can facilitate the determination of human health status and provide predictive information to prevent disease. For example, temperature variations during sleep can be used to gauge the circadian phase, with important implications for the characterization and treatment of common sleep disorders associated with delayed sleep-wake phase, advanced sleep-wake phase, and jet lag (*10*–*12*). In addition, sustained pressures associated with prolonged durations in a given posture can lead to pressure ulcers, with rates of incidence that correspond to 4.5 to 7% of hospitalized patients and involve substantially increased costs of care and lengths of stay at the hospital (*13*–*15*). Measuring pressure at the skin interface while lying on a bed could provide critical information in this context, as an alert for the need for preventive action to avoid skin sores, irritation, and decubitus ulcers. Recent studies (*16*–*18*) report pressures measured over time at four skin locations and relate these data to the development of skin ulcers, but in nonideal physical formats and with limited spatial resolution. Traditionally, these sleep and pressure studies occur in research laboratories and require invasive technology (such as rectal probes), capture only a single or small number (2 to 8) of measurement sites on the skin, or use an infrared (IR) imaging system to examine bare regions of the skin (*19*–*24*). Precise measurement and diagnosis require alternative methods for accurate mapping of temperature and pressure across the body at high spatial resolution.

Here, we use NFC power delivery and data communication to a central acquisition/control system with long-range readers and rapid scanning through a large-scale collection of devices mounted on the body to provide continuous streams of data that can be assembled into spatiotemporal maps of physiological processes. Alternative approaches, ranging from bed-integrated sensors (*25*) to visual inspection methodologies (*26*) to single-point measurements of skin hydration (*27*), have some value, but none can track, as an example, key pressure or temperature ulcer-related variables at fixed locations across the body, over time, in large-scale, array-based formats.

RESULTS

Large-scale distributed arrays of wireless sensors for full-body spatiotemporal mapping

Figure 1A shows a conceptual schematic illustration of the system. Here, 65 wireless, skin-like, sometimes known as "epidermal," NFC devices are mounted on the skin over the human body for measuring parameters of interest in real time, using a multiplexed, wireless scheme and one or more reader antennas. On the basis of the known locations of the devices, time-dependent data captured in this manner can be rendered as

[1]Department of Materials Science and Engineering, University of Illinois at Urbana-Champaign, Urbana, IL 61801, USA. [2]Department of Mechanical Engineering, Ajou University, San 5, Woncheon-Dong, Yeongtong-Gu, Suwon 16499, Republic of Korea. [3]Department of Electronics Convergence Engineering, Kwangwoon University, Seoul, Republic of Korea. [4]Applied Mechanics Laboratory, Department of Engineering Mechanics, Center for Mechanics and Materials, Tsinghua University, Beijing 100084, China. [5]Department of Civil and Environmental Engineering, Mechanical Engineering, and Materials Science and Engineering, Northwestern University, Evanston, IL 60208, USA. [6]Departments of Materials Science and Engineering, Biomedical Engineering, Neurological Surgery, Chemistry, Mechanical Engineering, Electrical Engineering and Computer Science; Center for Bio-Integrated Electronics; Simpson Querrey Institute for Nano/Biotechnology; Northwestern University, Evanston, IL 60208, USA. [7]Neurology and Sleep Medicine Carle Physician Group, University of Illinois at Urbana-Champaign, Urbana, IL 61801, USA. [8]School of Materials Science and Engineering, Pusan National University, Busan 609-735, Republic of Korea. [9]Weldon School of Biomedical Engineering, School of Mechanical Engineering, Center for Implantable Devices, Birck Nanotechnology Center, Purdue University, West Lafayette, IN 47907, USA. [10]Department of Engineering Mechanics, Southeast University, Nanjing 210096, China.
*These authors contributed equally to this work.
†Corresponding author. Email: y-huang@northwestern.edu (Y.H.); jrogers@northwestern.edu (J.A.R.)

Fig. 1. Concept illustrations, exploded view schematic diagrams, and photographs of wireless, battery-free epidermal sensors used for full-body monitoring. (**A**) Illustration of a collection of thin, conformable skin-mounted sensors distributed across the body, with continuous, wireless transmission of temperature and pressure data in a time-multiplexed fashion. (**B**) Top-view photograph (scale bar, 8 mm) of a representative sensor [red, near-field communication (NFC) microchip and temperature sensor; blue, designed silicon membrane pressure sensor; green, external resistor; black, polydimethylsiloxane (PDMS) for encapsulation of sensor]. (**C**) Exploded view schematic illustration of the device structure. (**D**) Illustration of 65 wireless sensors mounted across the body, with corresponding photographs of devices at representative locations in insets. (**E**) Photographs of sensors at different locations on the front and back of the body. Red and green dashed boxes correspond to (D). (**F**) Photograph of 65 sensors that were used for experiments (scale bar, 16 mm).

spatiotemporal color plots mapped onto the body shape. Figure 1B provides a photograph of a representative device, consisting of a small-scale, unpackaged integrated circuit chip that provides the NFC communication capability, along with subsystems for wireless energy harvesting, temperature sensing, and analog-to-digital (A/D) conversion (ams AG; NFC die SL13A, 100 μm thick, 2.38 mm × 2.38 mm); a pressure sensor that exploits the piezoresistive response of an ultrathin layer of monocrystalline silicon patterned into a spiral shape (diameter, 6.6 mm; width, 250 μm); and a simple resistor (0.6 mm × 0.3 mm × 0.3 mm) selected to ensure that the response of the pressure sensor falls into a range compatible with the A/D converter.

A detailed, exploded view schematic illustration in Fig. 1C summarizes the layouts of these components, their interconnections with one another, and their integration with a magnetic inductive loop antenna that serves as a wireless interface to an external reader. The construction involves a multilayer stack of (i) an NFC chip, a loop antenna (Cu, ~5 μm thick; diameter, 16 mm; width, 75 μm), and a silicon pressure sensor; (ii) thin films of polyimide (PI; ~1.2 μm thick) as electrical insulators; (iii) an overcoat and a base of polydimethylsiloxane (PDMS; ~1 MPa) as encapsulation; and (iv) a biocompatible skin adhesive (Scapa; thickness, ~50 μm; low modulus, ~17 kPa). The overall soft, deformable construction affords skin-compatible mechanics, as described in the context of related devices with simple authentication functionality (*28*). The thin geometry of the PDMS base (~50 μm thick) minimizes the thermal equilibrium time of the temperature sensor with the skin. A hole in the tape that is aligned to the temperature sensor provides additional advantage in this sense. The PDMS overcoat is comparatively thick (50 to 300 μm) to provide robust, physical protection from the environment. Figure 1 (D to F) shows schematic illustrations and photographs of a large collection of devices positioned for full-body coverage.

Fundamental characteristics of skin-like wireless temperature and pressure sensors

Figure 2 summarizes the results of experimental measurements and modeling results for the key device characteristics. Temperature sensing used a resistance thermometer detector (SL13A) integrated into the NFC chip (*29*, *30*). The properties of the temperature sensor are defined by (i) the accuracy and precision of measurement, (ii) the effective thermal mass of the overall device, and (iii) the response time. After a simple calibration procedure (fig. S1), wireless recordings under controlled conditions at a sampling rate of a few hertz matched those obtained at the same location using an IR camera (fig. S2, A to C; sensitivity, 0.05°C) with differences of less than 0.04°C. Even during temperature transients, the data captured in these two ways were similar to within an average of ±0.2°C (fig. S2, D to J), thereby defining the precision of the sensor.

The thermal mass is an important parameter that influences the time response and determines the magnitudes of any perturbations to the natural skin temperature associated with the presence of the device. The overall area of a typical device is ~214 mm^2. In a spatially averaged sense, the materials include Cu (10 $\mu g/mm^2$; heat capacity, C = 386 $J \cdot kg^{-1} \cdot K^{-1}$ and density, ρ = 8920 $kg \cdot m^{-3}$), PDMS (340 $\mu g/mm^2$; C = 1380 $J \cdot kg^{-1} \cdot K^{-1}$ and ρ = 970 $kg \cdot m^{-3}$), PI (3 $\mu g/mm^2$; C = 1090 $J \cdot kg^{-1} \cdot K^{-1}$ and ρ = 1490 $kg \cdot m^{-3}$), and Si (6 $\mu g/mm^2$; C = 710$J \cdot kg^{-1} \cdot K^{-1}$ and ρ = 2330 $kg \cdot m^{-3}$). The calculated thermal mass per unit area of Cu, PDMS, PI, and Si are 0.4, 46.9, 0.4, and 0.4 $\mu J \cdot mm^{-2} \cdot K^{-1}$, respectively. The total thermal mass per unit area of the device is, therefore, 48.1 $\mu J \cdot mm^{-2} \cdot K^{-1}$. Although this number is considerably higher than that associated with the most advanced, wired epidermal temperature sensors (1.5 to 30 $\mu J \cdot mm^{-2} \cdot K^{-1}$) (*31*–*34*), it is lower than that of the skin itself (C = 3391 $J \cdot kg^{-1} \cdot K^{-1}$, ρ = 1109 $kg \cdot m^{-3}$, and thickness = 1 mm yield a thermal mass of ~380 $\mu J \cdot mm^{-2} \cdot K^{-1}$). Thermal imaging (Fig. 2A) indicated that the presence of the device does not perturb the natural temperature of the skin in the mounting location or in nearby regions.

The relatively small thermal mass and overall construction also yield sensor response times that are only limited by the dynamics of thermal diffusion from the skin, through the base PDMS, and into the embedded temperature sensor in the NFC chip. As shown in Fig. 2A, a sensor cooled to 23°C and placed on the ventral side of the right forearm can be used to quantify the time for thermal equilibration between the skin and the sensor as a function of a representative design characteristic (thickness of the base PDMS). For thicknesses of 50, 100, and 200 μm, the equilibration times are 0.8, 1.5, and 2.5 s, respectively, as determined by wireless data acquisition at a sampling rate of 25 Hz. These values were consistent with those determined by finite element analysis (FEA; fig. S3) and the experiment (Fig. 2B). As the thickness of the bottom encapsulation layer decreases, the steady-state temperature of the chip approaches that of the adjacent material (33.89°, 33.81°, and 33.66°C for 50-, 100-, and 200-μm-thick bottom encapsulation layers, respectively). In addition, a device with a 50-μm-thick bottom encapsulation layer reaches the steady-state temperature faster than those with layers that have thicknesses of 100 or 200 μm. Such capabilities are sufficient to capture thermal transients relevant to most naturally occurring body processes, including respiration. A device mounted onto the skin of the upper lip, with the sensing region aligned to the base of the nostril, showed cyclical variations in temperature from 35.5°C during exhalation to 35.1°C during inhalation with results captured at a sampling rate of 6 Hz in an ambient laboratory environment and time-synchronized with respiration at four breaths per 10 s (Fig. 2, C and D).

The pressure sensor provides additional measurement functionality in the same device platform. Here, a spiral structure constructed from a thin, monocrystalline membrane of silicon (fig. S4, A and B) serves as the pressure-sensing element through its piezoresistive properties, in which the resistance changes with mechanical strain. The spiral shape facilitates stable operation on the surface of the skin due to enhanced uniformity in pressure-induced distributions of strain compared to those associated with simple, linear designs (fig. S4, C and D). Figure 2E shows the strain distributions obtained by FEA for pressure applied to devices with and without a thin overlayer of polyethylene terephthalate (PET; thickness, 5 μm; modulus, ~4.5 GPa) in the region of the silicon spiral structure, each deployed on the skin modeled with different characteristic moduli. The PET reduces the magnitude of the response and enhances the uniformity of the pressure distribution, providing a simple means for adjusting the range of sensitivity through material choices and device designs. For skin moduli of ~100 and ~200 kPa (*35*, *36*), the strain distributions in the silicon are comparable (~15% differences in average strain). The mechanism of strain generation and resistance change under uniform normal force (~10 kPa) arises mainly from Poisson effects associated with the encapsulating PDMS layers and consequent stretching of the spiral silicon structure, as opposed to bending deformations (fig. S5). The strain induced by applied pressure is insensitive to that associated with any initially bent state (fig. S6).

A simple empirical calibration procedure defines the connection between wireless measurements from a device and the actual pressure. Here, the PDMS layers protect the device while allowing soft, conformal contact to the skin (Fig. 2F). A voltage divider (Fig. 2G) converts the change in resistance into a voltage output for analog input to the A/D converter via the internally rectified output voltage of the NFC chip (V_{ext}), a negative supply or ground at the chip (V_{ss}), the analog input of the chip (S_{ext}), an external tuning resistor (R_2), and the pressure sensor (R_0), according to:

$$S_{ext} = \frac{(V_{ext} \times R_0) + (V_{ss} \times R_2)}{R_0 + R_2} \quad (1)$$

The chip requires the analog input (S_{ext}) to the A/D converter to lie between 0.3 and 0.6 V. Proper selection of the tuning resistor (R_2) ensures this condition for an operating range of interest. Measuring transient pressures—for example, a finger contact—may require a different external tuning resistor (R_2) than measuring large, sustained pressures—for example, human's weight. External force applied to a device via finger poking, touching, and holding yielded expected responses (Fig. 2H). For a given design, calibration procedures allow for accurate measurement across a range of pressures with negligible

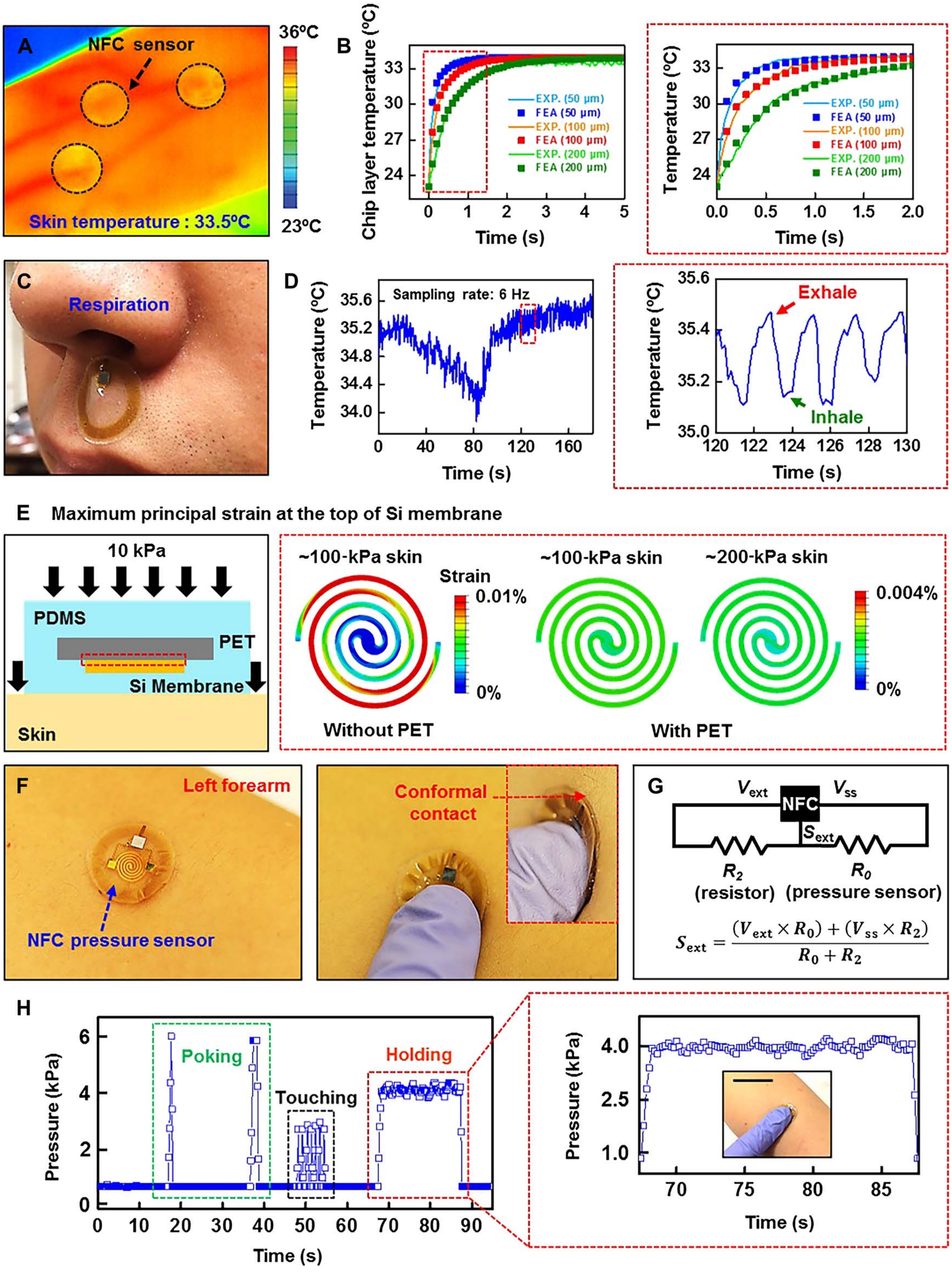

Fig. 2. Physical properties and measured responses of the sensors. (**A**) Infrared (IR) photograph of several sensors on the forearm of a human subject for measurement of temperature response time between the skin and sensor. (**B**) Measured and computed temporal responses of devices constructed with different thicknesses of an insulating elastomeric support, with enlarged view (right) of a region highlighted by the red dashed box. (**C**) Photograph of a device mounted on the upper lip of a human subject during respiration. (**D**) Temperature fluctuation wirelessly recorded (sampling rate, 6 Hz) with the device shown in (C), with enlarged view (right) of a region highlighted by the red dashed box. Cycles of inhalation (green arrow) and exhalation (red arrow) are evident. (**E**) Schematic diagram of the mechanics and finite element analysis (FEA) results for the maximum principal strain (enlargement of red dashed box, right) across the spiral-shaped thin silicon pressure sensor with and without the polyethylene terephthalate substrate. (**F**) Photographs of a sensor mounted on left forearm (left) and pressed with a fingertip (right). The inset shows a magnified view to highlight the conformal contact with the skin. (**G**) Equivalent circuit diagram of the pressure sensing part of the device. (**H**) Pressure fluctuation wirelessly recorded (sampling rate, 6 Hz) with a device on the left forearm during application of various forces with the fingertip (green dashed box, poking; black dashed box, touch; red dashed box, holding). The frame on the right corresponds to the red dashed box on the left, with inset photograph (scale bar, 4 cm).

hysteresis (fig. S7). Under continuous pressure (holding), the device has R_0 = 29.3 kilohms and R_2 = 220 kilohms. The measured voltage range (0.4 to 0.6 V) and corresponding resistance change (fig. S7A, $\Delta R/R$, ~1.2%) indicate pressures of a few kilopascals (poking, ~6 kPa; touching, ~3.2 kPa; holding, ~4.1 kPa; Fig. 2H).

Long-range wireless communication and power delivery and multiplexed readout

Because a typical sensor requires relatively small power for operation [standby, 2 μA at 1.5 V (~3 μW); operating, 150 μA at 1.5 V (~225 μW)], a standard smartphone can be used as a reader over distances of a few centimeters (Fig. 3A, movie S1, and fig. S8) (*37*). Full-body coverage can be accomplished with one or more large-scale loop antennas and external radio frequency (RF) power supplies (*P*, typically a few watts; movie S2). The operating range depends on the sizes and numbers of reader antennas, the RF power supplied to them, the sizes of the sensor antennas, and their angular orientation relative to the reader (*38*). Increasing the tilt angle of the sensor changed the maximum distance over which the signal can be detected only slightly for devices at the edge of the antenna; those at the center and corner regions show decreases in this distance by ~25% for the 60° tilt compared to the 0° tilt cases (fig. S9). Using two separate reader antennas next to each other allowed for full-body coverage (Fig. 3, B and C). For this multiplexed operation, communication and power delivery occurred to 65 separate sensors in a time sequential manner, continuously, such that all 65 sensors were read within 3 s. In addition, the NFC platform relies on the ISO/IEC 15693 standard, with a 10-bit analog-digital converter. Digital operation and sequential data acquisition across the array of devices minimize electronic noise and the influence of external or device-to-device electromagnetic interference.

Figure 3D and fig. S10 show measurements of range for various locations at different power levels. In all the cases, the central region of the antenna supports the longest range. The range *Z* for a sensor oriented parallel to the reader antenna (0° tilt) was 12 and 32 cm for RF power *P* of 4 and 12 W, consistent with the scaling law. Comparison calculations of the corresponding magnetic field strengths are shown in Fig. 3E and fig. S10 (C and D). At positions near the antennas, the peak magnitudes and the nonuniformities of the field distributions tended to increase with decreasing size (Fig. 3, F and G, and fig. S11). For distances z > ~20 cm, the largest

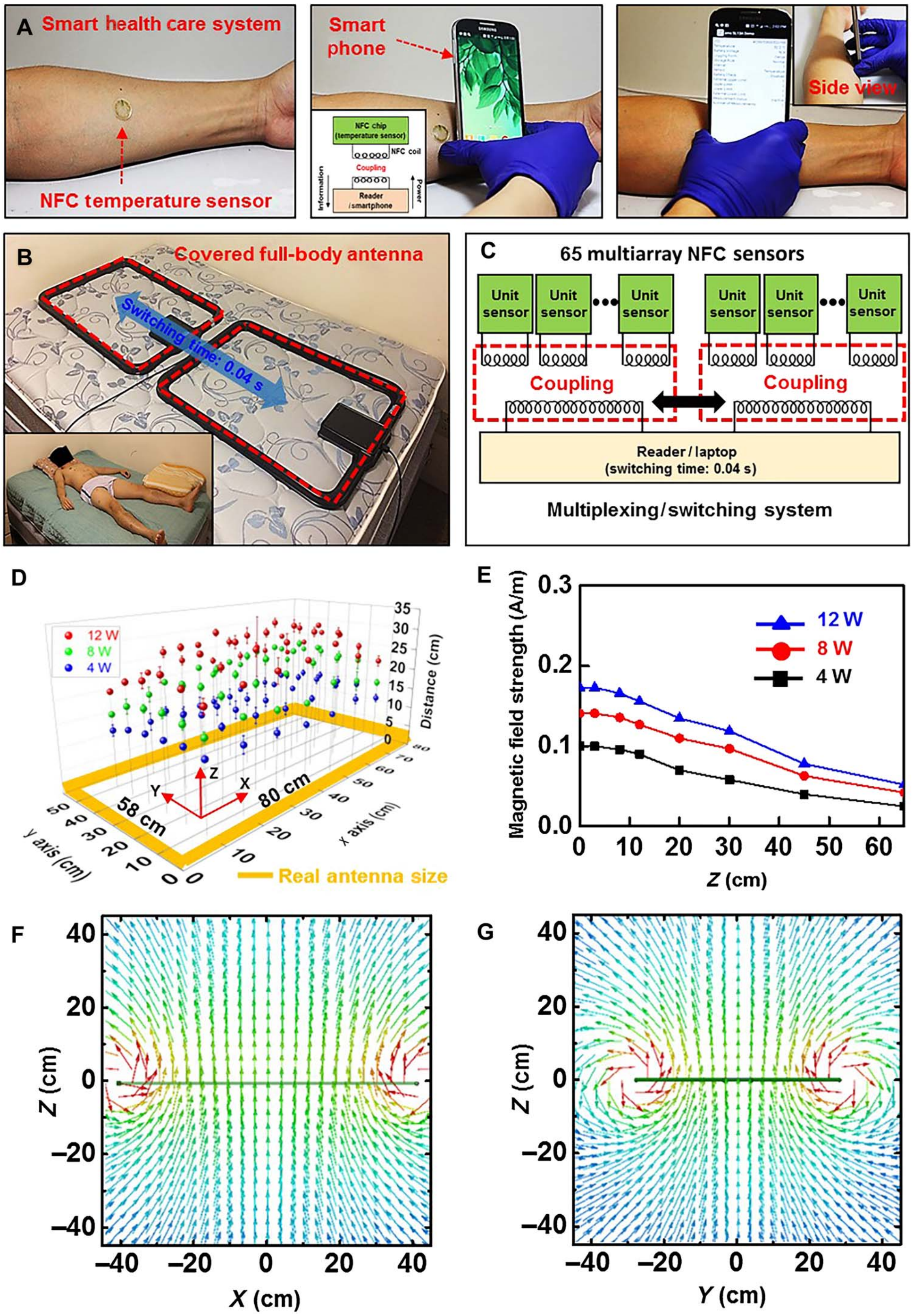

Fig. 3. Electromagnetic considerations in operating range and area coverage. (**A**) Sequence of photographs showing short-range readout from the skin-mounted sensor using a smartphone. Inset photograph is a diagram of the operational principles. (**B**) Photograph of dual-antenna system configured for full-body readout on a mattress, with inset of a subject lying on top of a ~5-cm-thick pad that covers the antennas. Subject: 27 years of age, male, 90 kg. (**C**) Diagram of use of such a system for time-multiplexed readout of a large collection of wireless sensors. (**D**) Graph of experimental measurements of operating range for an antenna (yellow rectangle in the *XY* plane) with dimensions of 800 mm × 580 mm × 400 mm, at radio frequency (RF) powers of 4, 8, and 12 W. (**E**) Computed magnetic field strength as a function of vertical distance (z) away from the *XY* plane at various RF powers. (**F** and **G**) Magnetic field distribution in *XZ* plane (F) and *YZ* plane (G).

antenna offered higher and broader coverage compared to the other options. For all cases (P = 4, 8, and 12 W), the computed range for the large (800 mm × 580 mm × 10 mm), medium (649 mm × 165 mm × 10 mm), and small (300 mm × 300 mm × 10 mm) antennas were comparable to experimental observations [Fig. 3D and figs. S10 (A and B) and S11, respectively]. A very large antenna (1600 mm × 580 mm × 10 mm) was considered, but the field strength was insufficient for ranges relevant to applications explored in human subject trials (fig. S12). For full-body coverage, using two separate, large reader antennas (800 mm × 58 mm × 10 mm) placed parallel in the xy plane and operated in a time-multiplexed manner was preferable. Simulation and experimental results indicated that the field strength with one antenna on and the other off was almost the same as that for a single isolated antenna (fig. S12, A and C).

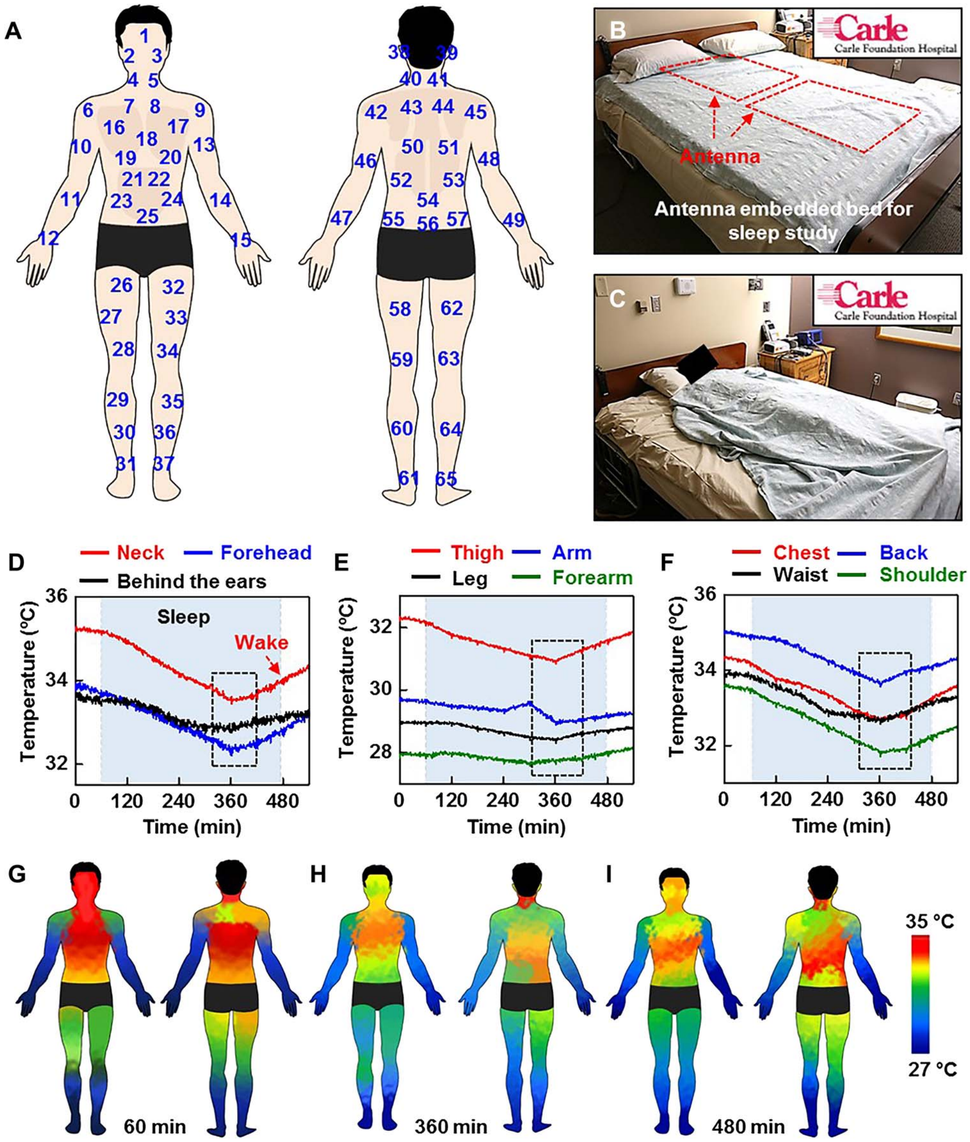

Fig. 4. Wireless, full-body thermography on a human subject in a clinical sleep laboratory. (**A**) Diagram of the locations of 65 sensors on the human body. (**B**) Photograph of the bed in the sleep laboratory, with a pair of readout antennas (red dashed boxes) located underneath a soft pad on the mattress. (**C**) Photograph of a subject lying on the mattress. Subject: 27 years of age, male, 90 kg. (**D** to **F**) Graphs of temperature averaged over local body regions during the 7 hours of the study. The gray shaded sections indicate sleep. The black dashed boxes indicate changes in temperature occurring 2 to 3 hours before waking. Number of sensors for average neck, 4; forehead, 3; behind the ears, 4, thigh, 10; arm, 4; leg, 10; forearm, 6; chest, 5; back, 8; waist, 7; shoulder, 4. (**G**) Maps of temperature distributions across the body just before the subject falls asleep, (**H**) 2 hours before waking, and (**I**) shortly after waking.

Full-body thermography in a clinical sleep laboratory

To investigate the utility of wireless sensing for full-body thermography, we performed studies with human subjects in a clinical sleep laboratory (photographs of clinical setup in fig. S13). First, 65 sensors were distributed across the body of a healthy 27-year-old male subject (Fig. 4A). As shown in Fig. 4 (B and C), two custom large-scale antennas constructed using small-diameter copper tubes (800 mm × 580 mm × 10 mm) residing under a pad (topper, ~5-cm thickness) were placed on top of the mattress (fig. S13). Full-body temperature mapping occurred 20 times per minute, continuously, during the course of the sleep study (9 hours). Wirelessly recorded temperatures are shown in Fig. 4 (D to F) and figs. S14 and S15. As expected, the core region of the body had a temperature of 2° to 3°C higher than the periphery (distant area from the heart). In most cases, body temperature begins to decrease at the onset of sleep (~60 min) and reaches a minimum value 2 to 3 hours before waking (*39*). Full-body heat maps assembled using the measured temperature data (Fig. 4, G to I, and fig. S16) confirm that the lowest body temperature occurred 2 to 3 hours before waking in our study.

To test the reliability of the sensors, devices mounted on the skin were monitored over a period of 3 days during which the subject participated in normal daily activities, including showering. Devices exhibited stable, reliable performance in measuring temperature and remained adhered to the skin (fig. S17A). Further confirmation of performance stability involved application of thermal stimuli (heat gun) on days 0 and 2 (maximum temperature, 33°C; sampling rate, 1 Hz), as well as on days 1 and 3 (maximum temperature, 30°C; sampling rate, 1 Hz), to verify proper operation over an extended period (fig. S17B).

Full-body pressure measurement in a hospital bed

Measuring pressure on the skin while lying on a bed could provide critical information as an alert for the need for preventive action to avoid skin sores, irritation, and decubitus ulcers. According to recent studies (*16–18*), pressures over 32 to 60 mmHg are problematic in this context. Comorbidities such as diabetes could lower thresholds depending on the site.

To test the ability of our wireless sensors to detect pressure at different anatomical locations in a hospital environment, we mounted 29 NFC pressure sensors on the dorsum of a healthy human subject with specific positions as indicated (Fig. 5, A and B). Pressure data were wirelessly recorded (sampling rate, 4 Hz) with the healthy human subject at supine angles of 0°, 30°, and 60° on an adjustable hospital bed (Fig. 5, C and D). Increased average pressure on the shoulder, buttocks, and dorsum was seen with increasing angle of the bed [Fig. 5 (E to H), fig. S18, and the raw data shown in figs. S19 to 21]. Color maps for pressures at various body positions are shown in Fig. 5 (I to K). The recorded pressures aligned with expectation and were consistent with literature data obtained using a measuring sheet with conventional wired sensors (*40*). In addition to average and time-integrated values, the sensors could capture changes in pressure in real time, associated with minor movements of the subject, thereby offering additional utility in sleep monitoring (fig. S19).

Additional experiments to compare against existing technologies

As summarized in Figs. 6 and 7, we conducted additional human (male, 54 and 32 years old; mass, 62 and 61 kg) experiments to compare our results with those obtained using gold standard clinical techniques, including IR skin thermography, rectal probes, and wired pressure sensors. Through Fig. 6 and figs. S22 and S23, the results correspond to temperature recordings for 480 min over two nights during the subject's habitual sleep period, in the supine position using 10 sensors. Figure 6 (A to C) and fig. S22 (A and B) summarize the setup in a clinical sleep laboratory at Carle Hospital, the configuration of the sensors, and various representative results. A large-range reader system captured temperature readings from eight wireless sensors attached to the back (shoulder, 1 to 3; thoracic, 4 to 6; lumbar, 7 and 8). Readings from the forehead (9) and right and left biceps (10 and 11) were collected using a smartphone, also every 15 min for 8 hours. Simultaneously, the temperature of these same regions was measured with an IR camera as a point of comparison. A commercial rectal

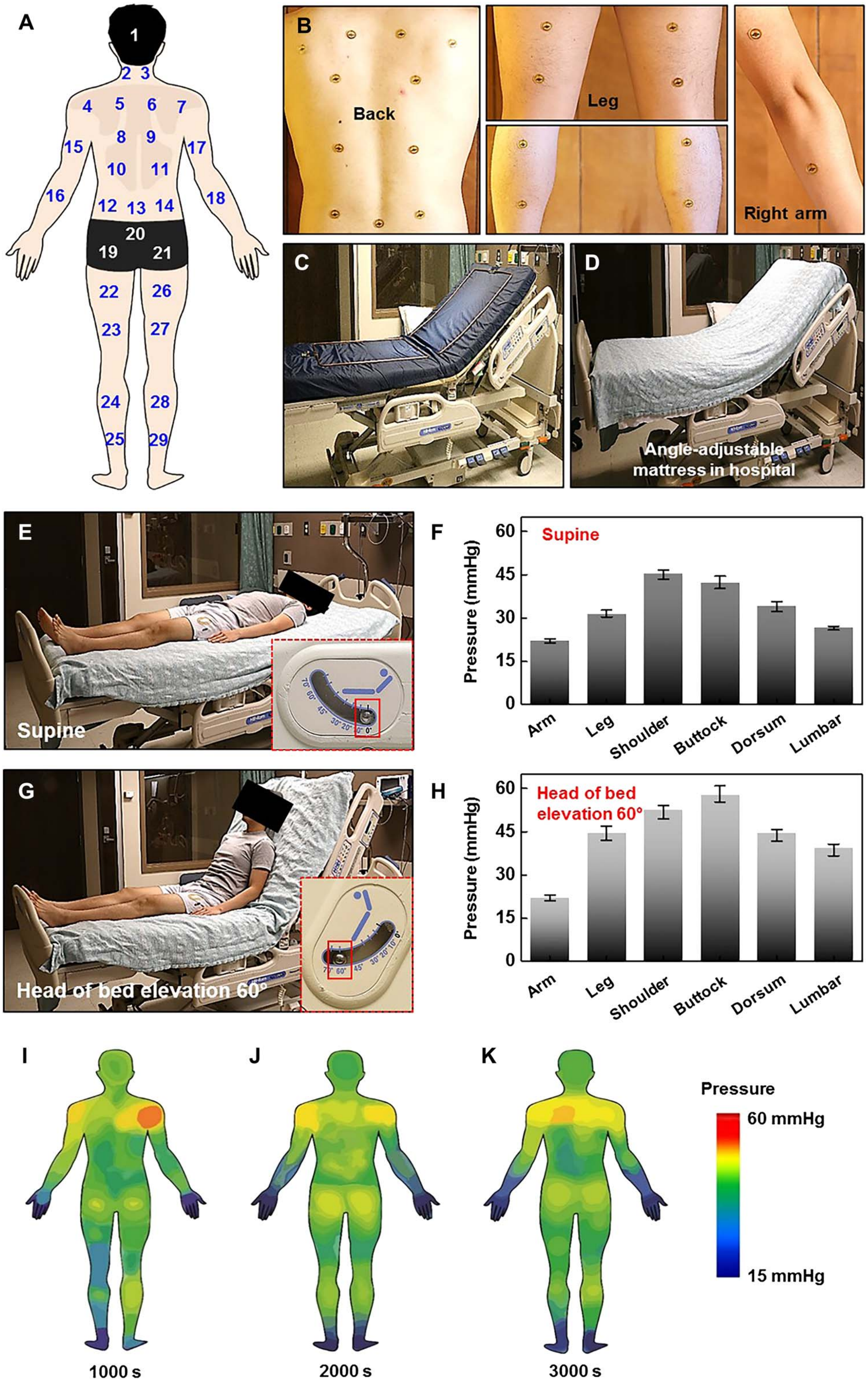

Fig. 5. Wireless, full-body pressure mapping on a human subject in a hospital bed. (**A** and **B**) Diagram and photographs of the locations of 29 sensors on the back side of the body. (**C** and **D**) Photograph of an angle-adjustable bed in a hospital, with dual-antenna setup for continuous pressure monitoring. (**E**) Photograph of a subject (27 years of age, male, 90 kg) lying on the bed in the supine position. (**F**) Corresponding results of pressure measurements averaged over the body region. Number of sensors for average arm, four; leg, four; shoulder, four; buttock, three; dorsum, four; lumbar, three. Error bar: SD, one set. (**G** and **H**) Photograph of a subject and pressure measurements for the supine angle of 60°. (**I**) Maps of pressure distributions across the body in supine position 0° after 1000, (**J**) 2000, and (**K**) 3000 s.

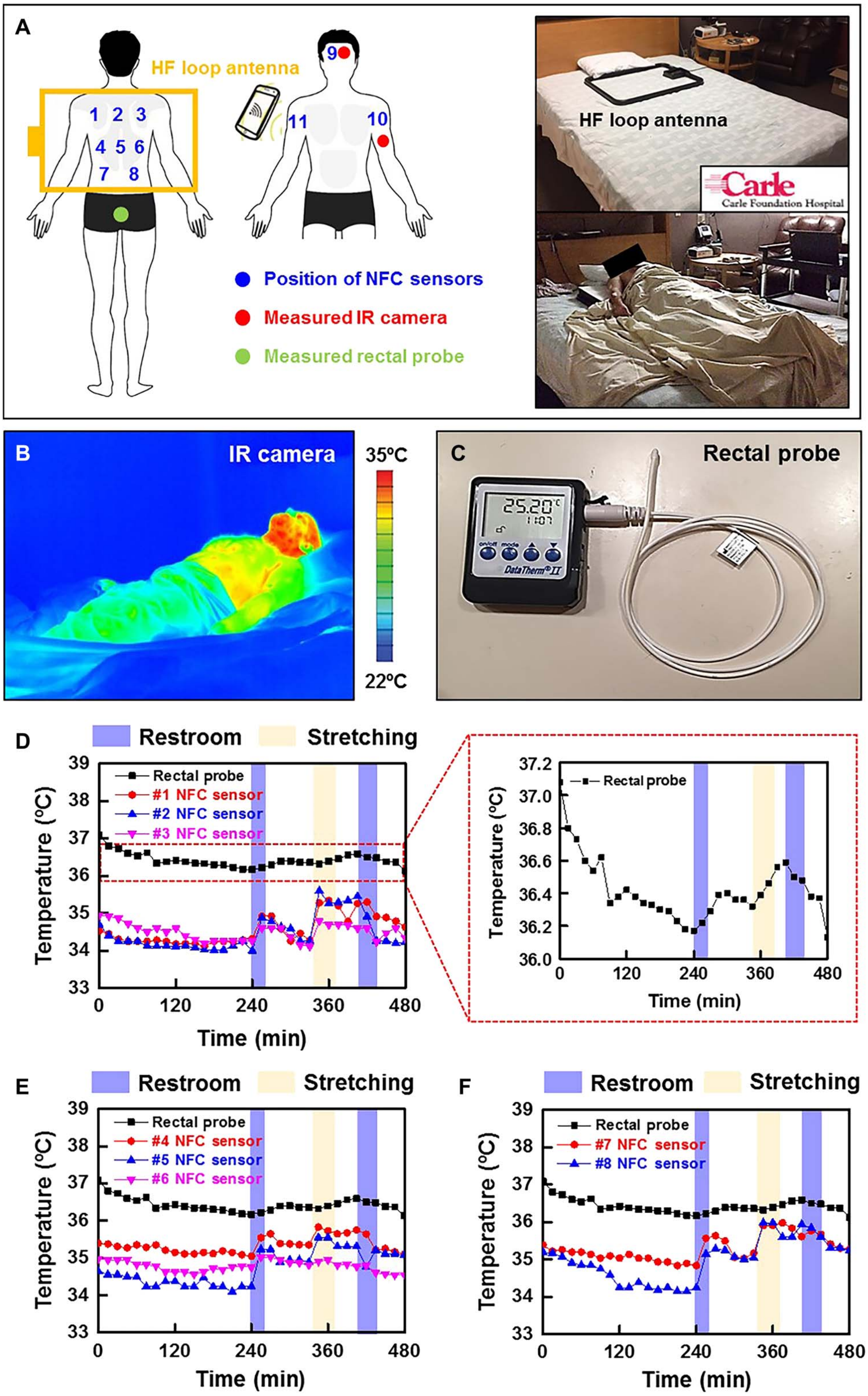

Fig. 6. Summary of comparative studies of temperature measurements on a human subject in a clinical sleep laboratory: first night. (**A**) Schematic illustration and photographs of the locations of sensors for temperature measurement, the associated reader equipment, and the subject lying on the bed in the supine position. (**B**) Thermal IR photograph of the subject. (**C**) Rectal probe equipment as a reference. (**D**) Temperature in the shoulder region captured using wireless sensors. The graph on the right shows temperature measured using the rectal probe (data with individual sensor). (**E** and **F**) Temperature in the thoracic and lumbar regions captured using wireless sensors (data with individual sensor).

probe measured the subject's core temperature.

Figure 6 (D to F) and fig. S22C summarize data collected during the first night. Figure 6D shows wirelessly recorded temperature values from the shoulder along with readings from the rectal probe. The blue and yellow highlighted regions correspond to the subject using the restroom and stretching, respectively. Expected changes in skin temperature coincide with these events. The inset shows that measurements with the rectal probe exhibit similar features. Overall, the data in Fig. 6 (E and F) and fig. S26 (A to C) indicate that the temperature gradually decreases from an initial value until the subject uses the restroom (240 min), with similar trends from the wireless skin temperature sensors and the rectal probe. Figure S22C summarizes temperatures of the forehead and the biceps recorded using the IR camera and the wireless sensors. The modest differences (less than 0.5°C) here are due mainly to slight spatial offsets (~1 cm) between the location of the IR measurement and that of the wireless sensors. Because the subject slept in the supine position and the bed provided insulation over the back, fluctuations in temperature are greater on the front side of body than the back, as might be expected. Figure S23 summarizes the setup and the measurement results for the second night. Compared to the first night, (i) the subject remained asleep for nearly 8 hours, and (ii) an additional wireless sensor was attached on the neck, adjacent to the carotid artery, to better approximate the core temperature. Detailed results of second night are shown in the Supplementary Materials.

Figure 7 shows the results of tests of wireless pressure sensors, with comparison to readings obtained using a commercial, wired sensor. As shown in Fig. 7 (A and B), seven wireless sensors were mounted on the back (shoulder, #1 and #2; dorsum, #3 and #4; lumbar, #5 to #7) using the same experimental setup as for the temperature tests. Figure 7 (C to E) shows some resulting data for the subject in the supine position. As expected, the bony prominences of the shoulder produced the highest pressures (shoulder pressure, 46 to 59 mmHg, wireless sensors #1 and #2). The error bars correspond to the range of changes associated with motion during the study. The dorsum

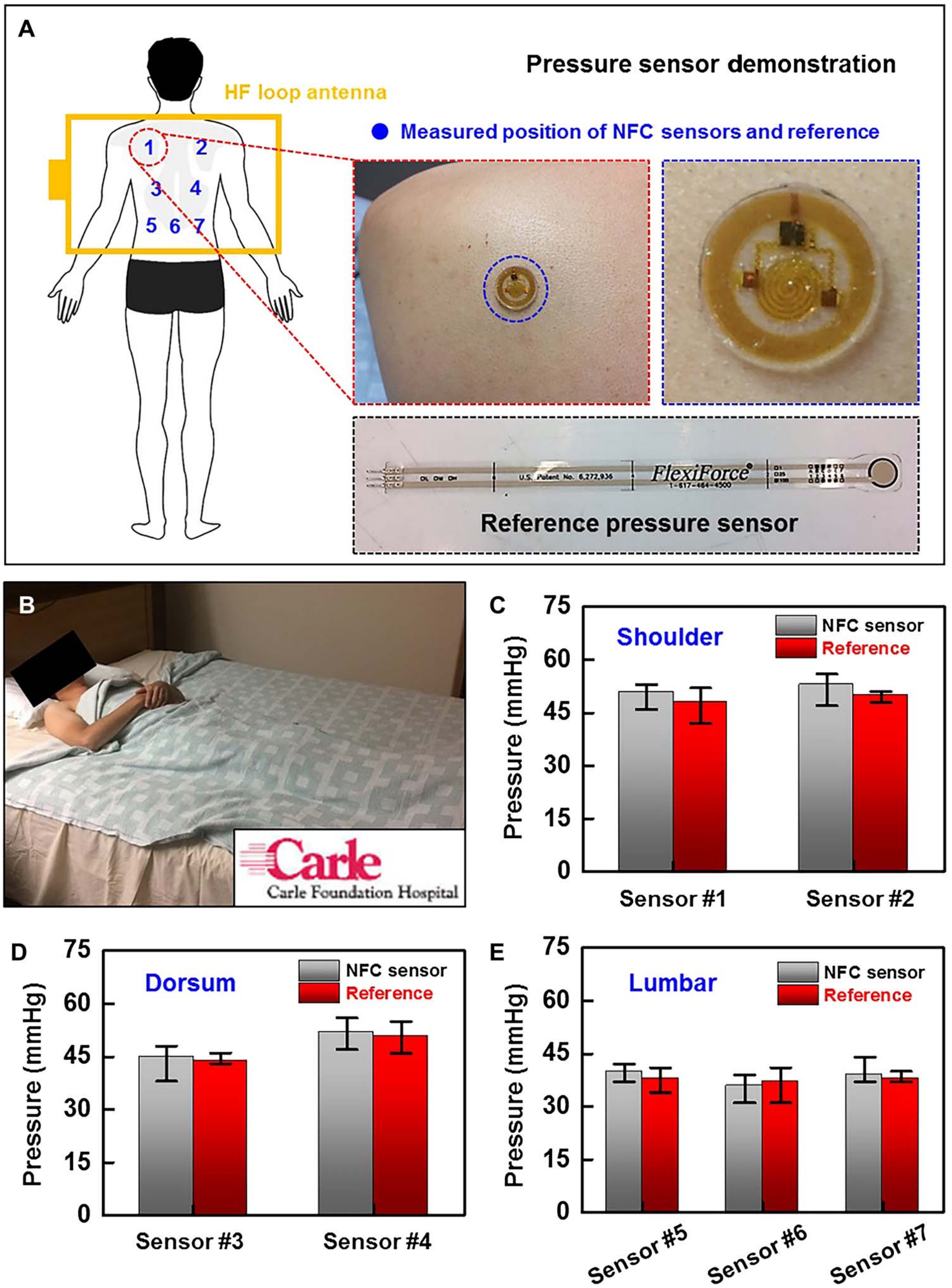

Fig. 7. Summary of comparative studies of pressure measurements on a human subject in a clinical sleep laboratory. (**A**) Schematic illustration and photographs of the positions for measurements of pressure using wireless sensors and a commercial, wired device (reference). (**B**) Photograph of the subject lying on the mattress with antenna embedded. (**C**) Pressure measured from the shoulder regions using wireless sensors and a reference device (measured at intervals of 1 min for 3 hours, data with individual sensor; error bar: SD, three sets). (**D**) Pressure measured from the dorsum region using wireless sensors and a reference device (measured at intervals of 1 min for 3 hours, data with individual sensor; error bar: SD, three sets). (**E**) Pressure measured from the lumbar region using wireless sensors and a reference device (measured at intervals of 1 min for 3 hours, data with individual sensor; error bar: SD, three sets).

region yielded lower pressures than shoulders (dorsum pressure, 38 to 48 mmHg, wireless pressure sensors #3 and #4), and the lumbar region exhibited the lowest pressures (lumbar pressure, 31 to 42 mmHg, wireless pressure sensors #5 to #7). In all cases, the wireless pressure measurements are consistent with those from the commercial reference sensor and with previously published clinical studies (*40*–*44*). These clinical, comparative tests show that the performance characteristics of our wireless sensors are similar to those of commercial devices, including systems used for clinical care. The standard approaches, however, have significant disadvantages. IR thermography can only measure from exposed regions of the skin, and the results often suffer from significant motion artifacts. Rectal probes are typically not acceptable for routine use, especially in sleep studies, because they can disrupt normal patterns of sleep. Currently available pressure sensors require wired readout, and they do not provide soft interfaces to the skin.

From these proof-of-concept experiments, we conclude that it is feasible to use these wireless sensors in a home setting because (i) the devices are simple to use, mounting and adhering to the body in a familiar manner much like a bandaid; and (ii) the external electronics are adapted from standard, commercially available platforms currently in widespread use as radio frequency identification (RFID) tag readers in theme parks, sports stadiums, libraries, and other similar locations. A demonstration of compatibility of the sensors with a gate-type RFID system (FEIG) is shown in fig. S24. Integration of such technology into the mattress of a bed is straightforward.

DISCUSSION

This paper demonstrates capabilities for full-body pressure and temperature monitoring using wireless, skin-adherent sensors in healthy human subjects in sleep laboratory and hospital settings. These thin, skin-like devices can precisely measure local pressure and temperature, as validated through computational modeling and comparison to experimental controls. Simultaneous wireless operation of 65 distinct sensors on discrete locations across the limbs, torso, neck, and head illustrates the possibilities for full-body pressure and temperature monitoring. Single or multiple large-scale loop antennas interfaced to RF power delivery and data acquisition electronics allow multiplexed operation with a range of tens of centimeters. The thin, soft construction of the devices and their battery-free operation allow their integration with the skin in a comfortable, physically "imperceptible" fashion with the ability to function for multiple days, including throughout a range of normal daily activities such as showering, without any irritation associated with mechanical or thermal loads.

Several clinical and engineering considerations favor a network of skin-deployed pressure and temperature sensors, especially those that are precise and accurate and locked to specific targeted regions of the body in ways that are difficult or impossible to reproduce with other approaches. For example, bed-integrated sensors cannot follow patient movements and therefore are unable, with certainty, to track pressure or temperature at any given anatomical location. In addition, their accuracy is compromised by additional confounders such as bed linens or mattresses. The results presented here illustrate advantages of wireless, skin-like sensors compared to these and other alternatives, such as IR temperature sensing, in two clinically relevant applications. The first is in full-body thermography for monitoring circadian phase, with potential in sleep studies, tumor detection, and hypothermia therapy. The second is in full-body pressure measurements that can serve as warning systems to prevent exposure to excessive, prolonged pressures that can lead to skin sores and decubitus ulcers. The basic sensor platforms are compatible with many additional types of functionality, including, but not limited to, measurements of electrophysiology, blood oximetry, core temperature, heart and respiration rate, and photoplethysmography. Exploiting these modalities and combining them with other sensing and actuating functionality represent promising directions for additional research. In the home setting demonstration, other modes of operation could involve readers along hallways or doorways, or integrated into chairs, using the frame as a support for the antenna and the base or back of the chair for the electronics.

The cost structures and methods of integration allow one-time, disposable modes of use, thereby increasing the breadth of clinical scalability and facilitating maintenance. For example, multiple sterilized sensors can be deployed and disposed of after use on an individual patient, thereby negating the need for expensive bed maintenance and laborious sterilization procedures of the sensors between uses. In addition, the sensors can function across multiple clinical scenarios including the intensive care unit, outpatient nursing homes, and assisted living locations. In all cases, the sensors move with the patient and are therefore compatible with transfers for radiological tests, physical therapy, or bathroom use—circumstances that can lead to deleterious pressures. A network of sensors has the ability to survey the entire patient, over time, with the potential to significantly reduce the nursing labor required.

Ongoing work focuses on scaled clinical studies with statistically significant numbers of actual patients, as an extension of the proof-of-concept demonstrations reported here. The results of such studies will provide insights into means for using data collected using the platforms introduced here to improve health outcomes. In terms of technology development, advanced wireless techniques and antenna designs may enable significant increases in operating range and decreases in required power, thereby overcoming some practical limitations associated with the range (~30 to 40 cm) and power (several watts) reported here. Improved sensitivity in detection may allow the use of thin metal films in place of the silicon membranes for the pressure sensors, with the potential to reduce the costs and improve the mechanical robustness.

MATERIALS AND METHODS

Study design

Here, we designed, fabricated, and tested wireless, flexible, skin-adherent sensors and antenna systems for pressure and temperature monitoring using NFC technology. The temperature sensor uses a resistance-based measurement system embedded in the NFC chip itself. The pressure sensors use spiral-shaped silicon membranes, for which changes in pressure induce changes in resistance associated with the piezoelectric effect. Studies with human subjects defined the accuracy and precision of the measurements in practical settings, as well as capabilities for continuous monitoring across multiple sites across the body. Approvals were obtained from the Carle Foundation Hospital and University of Illinois Institutional Review Boards. Human subject studies involved monitoring pressure and temperature during sleep in hospital settings. We also tested multiplex antenna systems in several configurations. The flexible sensors were compared to commercial temperature (IR camera, rectal probe) and pressure (FlexiForce device) measurement systems.

Fabrication of wireless NFC sensors

The fabrication began with spin-coating a layer of PI (1.2 μm; Microsystem) on a copper foil (Cu; 5 μm), as the first step in defining the loop antenna. Laminating the sheet, with PI side down, onto a glass slide coated with PDMS (Sylgard 184, Dow Corning; mixed at a 30:1 ratio of base to curing agent by weight, ~1 MPa) prepared the structure for photolithography and wet etching to create the loop (diameter, 16 mm; width, 75 μm). Another layer of PI (1.2 μm) uniformly spin-cast on top served as an encapsulation layer. Photolithography and dry etching [RIE; 20-sccm (standard cubic centimeter per minute) O_2, 200 mtorr, 150 W, 900 s] created small vias through the PI at each end of the loop for electrical connection. Electron beam evaporation formed another layer of Cu (1 μm). Photolithography and wet etching defined traces and contacts through the vias. Spin-casting yielded an additional coating of PI (1.2 μm). Electron beam evaporation, photolithography, and dry etching (RIE; 20-sccm CF_4, 50 mtorr, 100 W, 10 min) defined a hard mask of SiO_2 (50 nm). Further dry etching (RIE; 20-sccm O_2, 300 mtorr, 200 W, 1800 s) removed the exposed regions of the PI to create openings for electrical connection to the NFC die. A cellulose-based, water-soluble tape (Aquasol Corporation, ASWT-2) enabled retrieval of the resulting structure from the PDMS/glass substrate. Electron beam evaporation of a uniform layer of Ti/SiO_2 (5 nm/100 nm) onto the backside of this structure followed by exposure to ultraviolet-induced ozone facilitated strong bonding to a base layer of PDMS. After removal of the water-soluble tape, application of an In/Ag-based solder (Indium Corporation, 290, 180°C) established a mechanical and electrical interface between a thin (1 to 2 μm) NFC bare die, the loop antenna, and traces that lead to the components for pressure sensing.

A separate set of fabrication steps outlined below yielded a p-doped thin membrane of silicon in the shape of a spiral on a film of PET (SKC Corporation) for the pressure sensor. Silver epoxy (Ted Pella Corporation) bonded this sensor and external resistor (0.6 mm × 0.3 mm × 0.3 mm) to corresponding electrode pads. An additional layer of PDMS formed a top overlayer. Cutting through this layer and the base layer defined a disc shape with a slightly larger radius than the loop antenna.

Fabrication of p+-doped silicon pressure sensors

The fabrication, with details in the Supplementary Materials, began with p-doping the top silicon layer of silicon on insulator wafer. Undercut etching of the buried oxide layer followed by transfer printing integrated this silicon membrane onto a film of PET (thickness, 5 μm) coated with a layer (thickness, 1.5 μm) of epoxy (SU-8, MicroChem Corporation). Photolithography, followed by wet and dry etching, formed a spiral shape in the silicon. Electron beam evaporation, photolithography, and wet etching defined patterns of metal (Cr/Au; thicknesses, 13 and 150 nm) for contacts to the ends of the spiral. Spin-casting a layer of PI (thickness, 1.2 μm) and selective etching yielded an electrically insulating encapsulation layer with openings aligned to the metal contacts.

Characterization of the temperature sensors

A volunteer (male, 29 years old) reclined in a chair with his left forearm gently secured to the armrest. A wireless sensor placed on the ventral side of the left forearm provided continuous measurements of temperature. An IR camera placed 41 cm from the forearm, focused on the sensor as shown in Fig. 2A, yielded data for comparison. Additional tests with similar setups used three separate sensors laminated on the back of the hand. Here, measurements occurred during exposure to a temperature controlled heat gun (Milwaukee Corporation, 8988-20), as shown in fig. S2.

Tests of temperature changes associated with respiration

The studies involved a volunteer (male, 29 years old) seated on a chair with a wireless sensor laminated on the skin of the upper lip, just below the nostril. In an ambient laboratory environment, the measurements showed smooth oscillations between 35.5° and 35.1°C, time coincident with cycles of respiration, at a rate of four breaths per 10 s.

Characterization of the pressure sensors

The studies involved a volunteer (male, 29 years old) reclined in a chair with his left forearm gently secured to the armrest. An encapsulated pressure sensor placed on the ventral side of the left forearm, as shown Fig. 2F, captured variations associated with force applied with a fingertip. Qualitatively, the response correlated to the magnitude of the force, with larger values for poking and smaller ones for gentle touch and transients that correlated to the time duration of the applied force. Continuous pressure led to constant response. The resistances of the silicon pressure modules (R_0 = 29.3 kilohms) and the additional resistors (R_2 = 220 kilohms), together with the results of calibration in fig. S7A, can be used to determine the forces. The specific value of 29.3 kilohms in this circuit depends on various aspects of the fabrication of the silicon structures, but it is identical to within ±2 kilohms or 7% of the mean value associated with devices built in a single batch in our academic clean room facilities. The resistance of a sensor structure (R_1) with an unperturbed resistance of R_0 as a function of pressure can be approximated with an effective gauge factor (G), according to

$$R1 = R0(1 + G\varepsilon) \tag{2}$$

Here, the average strain along the length of the silicon membrane, ε, follows from FEA for 10-kPa pressure, as shown in fig. S25 (pressure applied locally on the device). The value of G extracted in this manner for the case of R_0 = 29.3 kilohms is in the range of ~50, comparable to intrinsic values expected for boron-doped silicon (*2*, *41*).

Measurement of the response time of pressure sensor

The response time to applied force can be quantified with a vibrating actuator stage and function generator (fig. S26). Figure S26A shows a schematic illustration of the placement of a wired silicon membrane pressure sensor and an actuator tip that can vibrate at selected frequencies (5, 15, 25, and 35 Hz). This platform provides reference data (resistance and voltage measurements) that are independent of the NFC electronics. The response time is in the range of a few tens of milliseconds, comparable to the peak sampling rate of our test electronics (fig. S26, C and D) and to recently reported metal, polymer, and carbon nanotube–based wired sensors (*42*–*46*).

Approaches for simultaneous measurement of temperature and pressure

The thermal sensor is insensitive to pressure because it is contained within the NFC chip via its internal functionality. Measurements show that the reading from this sensor does not depend on pressure, across a clinically relevant range, as might be expected based on the high-modulus, rigid nature of the chip. The pressure sensor has some finite-temperature response, but this part of the response can be easily removed by calibration procedures based on the readings from the temperature sensor. In this manner, the two sensors can yield separate, decoupled measurements of temperature and pressure. Relevant information appears in fig. S7.

Use in a clinical sleep laboratory

The studies involved a volunteer (male, 27 years old) with 65 wireless sensors mounted at locations across his entire body. Measurements were performed while sleeping on a mattress with a pair of reader antennas underneath in a sleep study laboratory at Carle Hospital (Carle and University of Illinois Institutional Review Boards, Carle IRB: 13113, UIUC IRB: 15112). Each sensor transmitted data for 0.045 s every 3 s from 10 p.m. to 7 a.m.

Use in a hospital room

The studies involved a volunteer (male, 29 years old, 90 kg mass) with 29 wireless sensors mounted at locations across his back. Measurements were performed to determine the pressure between his body and the mattress. As with the sleep studies, two large antennas embedded in the mattress allowed pressure measurements across the body for 0.25 s every 7.25 s during the experiments (~10 min).

Electromagnetic simulations

The FEA was adopted in the electromagnetic simulations to calculate the magnetic field distribution around reader antennas with different sizes (300 mm × 300 mm × 10 mm, 649 mm × 165 mm × 10 mm, and 800 mm × 580 mm × 10 mm). The simulations used the commercial software ANSYS HFSS, in which tetrahedron elements were used in the solution with adaptive meshing convergence (*47*). The default adaptive convergence condition, together with a spherical surface (1200 mm in radius) as the radiation boundary, ensured computational accuracy. The material parameters include the relative permittivity (ε_r), relative permeability (μ_r), and conductivity (σ) of the Cu, that is, $\varepsilon_{r\_Cu} = 1$, $\mu_{r\_Cu} = 0.999991$, and $\sigma_{Cu} = 5.8 \times 10^7$ S/m.

Additional sleep study experiment comparing with existing technology

Additional sleep studies involved 2 days with a volunteer (male, 54 years old, 62-kg mass) and 10 wireless sensors and a reference (Geschwenda, Data Thermal II model KD-2300) mounted at locations across the body. Measurements were performed while sleeping on a mattress with a reader antenna underneath in a sleep study laboratory at Carle Hospital. Each sensor transmitted data every 15 min for 8 hours. The pressure study involved a volunteer (male, 32 years old, 61-kg mass) with seven wireless sensors and wired pressure sensors (FlexiForce A201; thickness, 0.208 mm; length, 197 mm; width, 14 mm; sensing area, 9.53 mm) mounted at locations across the body. Each pressure sensor transmitted data every 1 min for 3 hours, repeated three times.

Statistical analysis

Data are presented as single values unless noted in the figure caption. Figures 5 and 7 show average values with the SD noted in the figure caption. Figure 4 also shows average values. Temperature deviations appear in fig. S2. Statistical analysis was not performed because of the small number of trials in this set of proof-of-concept experiments.

SUPPLEMENTARY MATERIALS

www.sciencetranslationalmedicine.org/cgi/content/full/10/435/eaan4950/DC1
Materials and Methods
Fig. S1. Process for calibrating the temperature sensors.
Fig. S2. Operation of calibrated wireless temperature sensors during rapid changes in temperature, with comparison to results obtained using an IR camera.
Fig. S3. Thermal FEA results as a function of thickness of the bottom PDMS layer.
Fig. S4. Photograph and structure schematic of silicon membrane, with comparison of pressure sensors with different shapes using FEA.
Fig. S5. Mechanism of strain generation in the sensor under uniform normal pressure.
Fig. S6. Effect of bending on the pressure sensor.
Fig. S7. Characterization of the boron-doped silicon pressure module.
Fig. S8. Screen view of temperature monitoring with a smartphone application in real time.
Fig. S9. Measurements of the effect of orientation under three power settings and representative positions.
Fig. S10. Measurements of operating distance for sensors placed at various locations inside each antenna with different power levels.
Fig. S11. Distributions of the magnetic field along the vertical direction for constant power (12 W) and different antenna sizes.
Fig. S12. Simulation of field strength of different antenna sizes and multiplexed operation.
Fig. S13. Embedded antenna setup for sleep studies at Carle Hospital.
Fig. S14. Results of sleep studies conducted with arrays of temperature sensors on the front of the body.
Fig. S15. Results of sleep studies conducted with arrays of temperature sensors on the back of the body.
Fig. S16. Color heat maps of the entire body constructed from temperature data collected using NFC sensors.
Fig. S17. Results of the sensors' lifetime during 3 days of continuous wear.
Fig. S18. Results of wirelessly recorded data obtained while lying at a supine angle of 30°.
Fig. S19. Graphs of pressure measurements in a hospital bed while lying at a supine angle of 0° (data with individual sensor).
Fig. S20. Graphs of pressure measurements obtained in a hospital bed while lying at a supine angle of 30° (data with individual sensor).
Fig. S21. Graphs of pressure measurements obtained in a hospital bed while lying at a supine angle of 60° (data with individual sensor).
Fig. S22. Summary of comparative studies of temperature measurements in a clinical sleep laboratory: first night.
Fig. S23. Summary of the experimental setup and data collected in comparative studies of temperature measurements in a clinical sleep laboratory: second night.
Fig. S24. Demonstration of a gate-type reader system and antenna.
Fig. S25. Strain distributions at the silicon layer induced by local pressure.
Fig. S26. Measurements of response time obtained using a vibrating actuator stage and a function generator.
Fig. S27. Mechanical response of an encapsulated sensor on a phantom skin under stretching, bending, and twisting.
Movie S1. Recordings from a single sensor captured using NFC between an epidermal device and a smartphone through a prosthetic.
Movie S2. Recordings from four sensors simultaneously using a large-scale (800 mm × 580 mm × 400 mm) RF antenna through a prosthetic.

REFERENCES AND NOTES

1. J. Kim, R. Ghaffari, D.-H. Kim, The quest for miniaturized soft bioelectronic devices. *Nat. Biomed. Eng.* **1**, 0049 (2017).
2. S.-K. Kang, R. K. J. Murphy, S.-W. Hwang, S. M. Lee, D. V. Harburg, N. A. Krueger, J. Shin, P. Gamble, H. Cheng, S. Yu, Z. Liu, J. G. McCall, M. Stephen, H. Ying, J. Kim, G. Park, R. C. Webb, C. H. Lee, S. Chung, D. S. Wie, A. D. Gujar, B. Vemulapalli, A. H. Kim, K.-M. Lee, J. Cheng, Y. Huang, S. H. Lee, P. V. Braun, W. Z. Ray, J. A. Rogers, Bioresorbable silicon electronic sensors for the brain. *Nature* **530**, 71–76 (2016).
3. S. K. Vashist, P. B. Luppa, L. Y. Yeo, A. Ozcan, J. H. Luong, Emerging technologies for next-generation point-of-care testing. *Trends Biotechnol.* **33**, 692–705 (2015).
4. W. Gao, S. Emaminejad, H. Y. Y. Nyein, S. Challa, K. Chen, A. Peck, H. M. Fahad, H. Ota, H. Shiraki, D. Kiriya, D.-H. Lien, G. A. Brooks, R. W. Davis, A. Javey, Fully integrated wearable sensor arrays for multiplexed in situ perspiration analysis. *Nature* **529**, 509–514 (2016).
5. S. R. Steinhubl, E. D. Muse, E. J. Topol, The emerging field of mobile health. *Sci. Transl. Med.* **7**, 283rv3 (2015).
6. E. Monton, J. F. Hernandez, J. M. Blasco, T. Hervé, J. Micallef, I. Grech, A. Brincat, V. Traver, Body area network for wireless patient monitoring. *IET Commun.* **2**, 215–222 (2008).
7. A. M. Hussain, F. A. Ghaffar, S. I. Park, J. A. Rogers, A. Shamim, M. M. Hussain, Metal/polymer based stretchable antenna for constant frequency far-field communication in wearable electronics. *Adv. Funct. Mater.* **25**, 6565–6575 (2015).
8. J. Kim, P. Gutruf, A. M. Chiarelli, S. Y. Heo, K. Cho, Z. Xie, A. Banks, S. Han, K.-I. Jang, J. W. Lee, K.-T. Lee, X. Feng, Y. Huang, M. Fabini, G. Gratton, U. Paik, J. A. Rogers, Miniaturized battery-free wireless systems for wearable pulse oximetry. *Adv. Funct. Mater.* **27**, 1604373 (2017).
9. H. Araki, J. Kim, S. Zhang, A. Banks, K. E. Crawford, X. Sheng, P. Gutruf, Y. Shi, R. M. Pielak, J. A. Rogers, Materials and device designs for an epidermal UV colorimetric dosimeter with near field communication capabilities. *Adv. Funct. Mater.* **27**, 1604465 (2017).
10. S. M. Abbott, K. J. Reid, P. C. Zee, Circadian rhythm sleep-wake disorders. *Psychiatr. Clin. North Am.* **38**, 805–823 (2015).
11. H. J. Burgess, J. S. Emens, Circadian-based therapies for circadian rhythm sleep-wake disorders. *Curr. Sleep Med. Rep.* **2**, 158–165 (2016).
12. M. A. Carskadon, S. E. Labyak, C. Acebo, R. Seifer, Intrinsic circadian period of adolescent humans measured in conditions of forced desynchrony. *Neurosci. Lett.* **260**, 129–132 (1999).
13. K. Whittington, M. Patrick, J. L. Roberts, A national study of pressure ulcer prevalence and incidence in acute care hospitals. *J. Wound Ostomy Continence Nurs.* **27**, 209–215 (2000).
14. C. H. Lyder, Y. Wang, M. Metersky, M. Curry, R. Kliman, N. R. Verzier, D. R. Hunt, Hospital-acquired pressure ulcers: Results from the national Medicare Patient Safety Monitoring System study. *J. Am. Geriatr. Soc.* **60**, 1603–1608 (2012).
15. R. M. Allman, P. S. Goode, N. Burst, A. A. Bartolucci, D. R. Thomas, Pressure ulcers, hospital complications, and disease severity: Impact on hospital costs and length of stay. *Adv. Wound Care* **12**, 22–30 (1999).
16. M. J. Grap, C. L. Munro, P. A. Wetzel, C. M. Schubert, A. Pepperl, R. S. Burk, V. Lucas, Tissue interface pressure and skin integrity in critically ill, mechanically ventilated patients. *Intensive Crit. Care Nurs.* **38**, 1–9 (2017).
17. J. Cox, L. Kaes, M. Martinez, D. Moles, A prospective, observational study to assess the use of thermography to predict progression of discolored intact skin to necrosis among patients in skilled nursing facilities. *Ostomy Wound Manage.* **62**, 14–33 (2016).
18. R. Behrendt, A. M. Ghaznavi, M. Mahan, S. Craft, A. Siddiqui, Continuous bedside pressure mapping and rates of hospital-associated pressure ulcers in a medical intensive care unit. *Am. J. Crit. Care* **23**, 127–133 (2014).
19. D. J. Dijk, C. A. Czeisler, Contribution of the circadian pacemaker and the sleep homeostat to sleep propensity, sleep structure, electroencephalographic slow waves, and sleep spindle activity in humans. *J. Neurosci.* **15**, 3526–3538 (1995).
20. C. Blume, J. Lechinger, N. Santhi, R. del Giudice, M.-T. Gnjezda, G. Pichler, M. Scarpatetti, J. Donis, G. Michitsch, M. Schabus, Significance of circadian rhythms in severely brain-injured patients: A clue to consciousness? *Neurology* **88**, 1933–1941 (2017).
21. M. Bracci, V. Ciarapica, A. Copertaro, M. Barbaresi, N. Manzella, M. Tomasetti, S. Gaetani, F. Monaco, M. Amati, M. Valentino, V. Rapisarda, L. Santarelli, Peripheral skin temperature and circadian biological clock in shift nurses after a day off. *Int. J. Mol. Sci.* **17**, E623 (2016).
22. M. J. Hasselberg, J. McMahon, K. Parker, The validity, reliability, and utility of the iButton® for measurement of body temperature circadian rhythms in sleep/wake research. *Sleep Med.* **14**, 5–11 (2013).
23. J. A. Sarabia, M. A. Rol, P. Mendiola, J. A. Madrid, Circadian rhythm of wrist temperature in normal-living subject: A candidate of new index of the circadian system. *Physiol. Behav.* **95**, 570–580 (2008).
24. S. B. Rutkove, A. Veves, T. Mitsa, R. Nie, P. M. Fogerson, L. P. Garmirian, R. A. Nardin, Impaired distal thermoregulation in diabetes and diabetic polyneuropathy. *Diabetes Care* **32**, 671–676 (2009).
25. P. Chung, A. Rowe, M. Etemadi, H. Lee, S. Roy, Fabric-based pressure sensor array for decubitus ulcer monitoring. *Conf. Proc. IEEE Eng. Med. Biol. Soc.* **2013**, 6506–6509 (2013).
26. S. D. Horn, P. Buerhaus, N. Bergstrom, R. J. Smout, RN staffing time and outcomes of long-stay nursing home residents: Pressure ulcers and other adverse outcomes are less likely as RNs spend more time on direct patient care. *Am. J. Nurs.* **105**, 58–70 (2005).
27. J. J. Harrow, H. N. Mayrovitz, Subepidermal moisture surrounding pressure ulcers in persons with a spinal cord injury: A pilot study. *J. Spinal Cord Med.* **37**, 719–728 (2014).
28. A. Koh, D. Kang, Y. Xue, S. Lee, R. M. Pielak, J. Kim, T. Hwang, S. Min, A. Banks, P. Bastien, M. C. Manco, L. Wang, K. R. Ammann, K.-I. Jang, P. Won, S. Han, R. Ghaffari, U. Paik, M. J. Slepian, G. Balooch, Y. Huang, J. A. Rogers, A soft, wearable microfluidic device for the capture, storage, and colorimetric sensing of sweat. *Sci. Transl. Med.* **8**, 366ra165 (2016).
29. IDS Microchip AG, Thermal Design Guideline for Wearable Devices, Date Sheet of AS62x0 (2016).
30. IDS Microchip AG, Smart Sensory Tag Chip For Unique Identification, Data Sheet of SL13A (2015).
31. Y. Zhang, R. C. Webb, H. Luo, Y. Xue, J. Kurniawan, N. H. Cho, S. Krishnan, Y. Li, Y. Huang, J. A. Rogers, Theoretical and experimental studies of epidermal heat flux sensors for measurements of core body temperature. *Adv. Healthc. Mater.* **5**, 119–127 (2016).

32. L. Gao, Y. Zhang, V. Malyarchuk, L. Jia, K.-I. Jang, R. C. Webb, H. Fu, Y. Shi, G. Zhou, L. Shi, D. Shah, X. Huang, B. Xu, C. Yu, Y. Huang, J. A. Rogers, Epidermal photonic devices for quantitative imaging of temperature and thermal transport characteristics of the skin. *Nat. Commun.* **5**, 4938 (2014).
33. R. C. Webb, A. P. Bonifas, A. Behnaz, Y. Zhang, K. J. Yu, H. Cheng, M. Shi, Z. Bian, Z. Liu, Y.-S. Kim, W.-H. Yeo, J. S. Park, J. Song, Y. Li, Y. Huang, A. M. Gorbach, J. A. Rogers, Ultrathin conformal devices for precise and continuous thermal characterization of human skin. *Nat. Mater.* **12**, 938–944 (2013).
34. R. C. Webb, Y. Ma, S. Krishnan, Y. Li, S. Yoon, X. Guo, X. Feng, Y. Shi, M. Seidel, N. H. Cho, J. Kurniawan, J. Ahad, N. Sheth, J. Kim, J. G. T. Taylor IV, T. Darlington, K. Chang, W. Huang, J. Ayers, A. Gruebele, R. M. Pielak, M. J. Slepian, Y. Huang, A. M. Gorbach, J. A. Rogers, Epidermal devices for noninvasive, precise, and continuous mapping of macrovascular and microvascular blood flow. *Sci. Adv.* **1**, e1500701 (2015).
35. C. H. Lee, Y. Ma, K.-I. Jang, A. Banks, T. Pan, X. Feng, J. S. Kim, D. Kang, M. S. Raj, B. L. McGrane, X. Wang, R. Ghaffari, Y. Huang, J. A. Rogers, Soft core/shell packages for stretchable electronics. *Adv. Funct. Mater.* **25**, 3698–3704 (2015).
36. Y. Liu, J. J. S. Norton, R. Qazi, Z. Zou, K. R. Ammann, H. Liu, L. Yan, P. L. Tran, K.-I. Jang, J. W. Lee, D. Zhang, K. A. Kilian, S. H. Jung, T. Bretl, J. Xiao, M. J. Slepian, Y. Huang, J.-W. Jeong, J. A. Rogers, Epidermal mechano-acoustic sensing electronics for cardiovascular diagnostics and human-machine interfaces. *Sci. Adv.* **2**, e1601185 (2016).
37. J. Kim, G. A. Salvatore, H. Araki, A. M. Chiarelli, Z. Xie, A. Banks, X. Sheng, Y. Liu, J. W. Lee, K.-I. Jang, S. Y. Heo, K. Cho, H. Luo, B. Zimmerman, J. Kim, L. Yan, X. Feng, S. Xu, M. Fabiani, G. Gratton, Y. Huang, U. Paik, J. A. Rogers, Battery-free, stretchable optoelectronic systems for wireless optical characterization of the skin. *Sci. Adv.* **2**, e1600418 (2016).
38. G. Shin, A. M. Gomez, R. Al-Hasani, Y. R. Jeong, J. Kim, Z. Xie, A. Banks, S. M. Lee, S. Y. Han, C. J. Yoo, Flexible near-field wireless optoelectronics as subdermal implants for broad applications in optogenetics. *Neuron* **93**, 509–521.e3 (2017).
39. M. Okawa, M. Uchiyama, Circadian rhythm sleep disorders: Characteristics and entrainment pathology in delayed sleep phase and non-24-h sleep-wake syndrome. *Sleep Med. Rev.* **11**, 485–496 (2007).
40. T. Defloor, The effect of position and mattress on interface pressure. *Appl. Nurs. Res.* **13**, 2–11 (2000).
41. S. M. Won, H.-S. Kim, N. Lu, D.-G. Kim, C. Del Solar, T. Duenas, A. Ameen, J. A. Rogers, Piezoresistive strain sensors and multiplexed arrays using assemblies of single-crystalline silicon nanoribbons on plastic substrates. *IEEE Trans. Electron Devices* **58**, 4074–4078 (2011).
42. S. Lee, A. Reuveny, J. Reeder, H. Jin, Q. Liu, T. Yokota, T. Sekitani, T. Isoyama, Y. Abe, Z. Suo, T. Someya, A transparent bending-insensitive pressure sensor. *Nat. Nanotechnol.* **11**, 472–478 (2016).
43. L. Pan, A. Chortos, G. Yu, Y. Wang, S. Isaacson, R. Allen, Y. Shi, R. Dauskardt, Z. Bao, An ultra-sensitive resistive pressure sensor based on hollow-sphere microstructure induced elasticity in conducting polymer film. *Nat. Commun.* **5**, 3002 (2014).
44. L. Y. Chen, B. C.-K. Tee, A. L. Chortos, G. Schwartz, V. Tse, D. J. Lipomi, H.-S. P. Wong, M. V. McConnell, Z. Bao, Continuous wireless pressure monitoring and mapping with ultra-small passive sensors for health monitoring and critical care. *Nat. Commun.* **5**, 5028 (2014).
45. T. Yamada, Y. Hayamizu, Y. Yamamoto, Y. Yomogida, A. Izadi-Najafabadi, D. N. Futaba, K. Hata, A stretchable carbon nanotube strain sensor for human-motion detection. *Nat. Nanotechnol.* **6**, 296–301 (2011).
46. N. Lu, C. Lu, S. Yang, J. Rogers, Highly sensitive skin-mountable strain gauges based entirely on elastomers. *Adv. Funct. Mater.* **22**, 4044–4050 (2012).
47. D. Simulia (Manchester, England: Hibbitt, Karlsson & Sorensen Inc., 2010).

Acknowledgments: We thank everyone who helped in our work. **Funding:** S.H. and D.K. were supported by the new faculty research fund of Ajou University and the Ajou university research fund. Y.M., Z.X., and X.F. acknowledge the support from the National Basic Research Program of China (grant no. 2015CB351900) and National Natural Science Foundation of China (grant nos. 11402135, 11402134, and 11320101001). Y.H. and J.A.R. acknowledge the support from the NSF (grant nos. DMR-1121262, CMMI-1300846, CMMI-1400169, and CMMI-1534120) and the NIH (grant no. R01EB019337). D.K. was supported by Basic Science Research Program through the National Research Foundation of Korea funded by the Ministry of Science, Information and Communications Technologies and Future Planning (2016R1C1B1009689). J.K. acknowledges the support from the Research Grant of Kwangwoon University in 2017. **Author contributions:** S.H., J.K., S.M.W., Y.M., Y.H., and J.A.R. led the development of the concepts, designed the experiments, interpreted the results, and wrote the paper. S.H., J.K., S.M.W., and Y.M. led the experimental works, with support from D.K., K.L., H.U.C., A.B., S.M., S.Y.H., J.W.L., C.-H.L., and B.H.K. as fabrication of several sensors and design of electric circuit. In addition, Z.X., K.L., Y.Z., C.W., and X.F. performed mechanical modeling and simulations. C.R.D. contributed to the organization and design of the human test in Carle Hospital and provided in-depth discussion. Y.H. and J.A.R. provided technical guidance. All authors contributed to proofreading the manuscript. **Competing interests:** J.A.R., S.H., S.M.W., and J.K. are inventors on Patent Cooperation Treaty Patent Application PCT/US18/15389 submitted by Northwestern University and The Board of Trustees of the University of Illinois that covers "Wireless surface mountable sensors and actuators." The other authors declare that they have no competing financial interests. **Data and materials availability:** All data needed to evaluate the conclusions are present in the paper and/or the Supplementary Materials. Additional information related to this paper may be requested from the authors.

Submitted 21 April 2017
Accepted 13 February 2018
Published 4 April 2018
10.1126/scitranslmed.aan4950

Citation: S. Han, J. Kim, S. M. Won, Y. Ma, D. Kang, Z. Xie, K.-T. Lee, H. U. Chung, A. Banks, S. Min, S. Y. Heo, C. R. Davies, J. W. Lee, C.-H. Lee, B. H. Kim, K. Li, Y. Zhou, C. Wei, X. Feng, Y. Huang, J. A. Rogers, Battery-free, wireless sensors for full-body pressure and temperature mapping. *Sci. Transl. Med.* **10**, eaan4950 (2018).

Science Translational Medicine

Battery-free, wireless sensors for full-body pressure and temperature mapping

Seungyong Han, Jeonghyun Kim, Sang Min Won, Yinji Ma, Daeshik Kang, Zhaoqian Xie, Kyu-Tae Lee, Ha Uk Chung, Anthony Banks, Seunghwan Min, Seung Yun Heo, Charles R. Davies, Jung Woo Lee, Chi-Hwan Lee, Bong Hoon Kim, Kan Li, Yadong Zhou, Chen Wei, Xue Feng, Yonggang Huang and John A. Rogers

Sci Transl Med **10**, eaan4950.
DOI: 10.1126/scitranslmed.aan4950

Feeling the heat under pressure
Pressure ulcers, or bedsores, can develop at skin sites overlying bony areas of the body when a patient remains in one position for an extended period. These sores can be difficult to detect in their early stages. To begin to address this, Han *et al*. developed flexible, adherent sensors that measure skin temperature and pressure in real time. The small sensors use wireless power to communicate with external reader antennas. Data acquired from multiple sensors were used to create full-body pressure and temperature maps, which detected changes in pressure due to adjusting the angle of hospital bed incline and changes in skin temperature during sleep in human participants during proof-of-concept studies.